PERGAMON

International Journal of Solids and Structures 40 (2003) 125–142

INTERNATIONAL JOURNAL OF SOLIDS and STRUCTURES

www.elsevier.com/locate/ijsolstr

Prediction of thermal crack spacing

D.H. Timm [a], B.B. Guzina [b,*], V.R. Voller [b]

[a] *Department of Civil Engineering, Auburn University, 238 Harbert Engineering Center, Auburn, AL 36849, USA*
[b] *Department of Civil Engineering, University of Minnesota, 500 Pillsbury Dr. S.E., Minneapolis, MN 55455, USA*

Received 11 December 2001; received in revised form 9 August 2002

Abstract

When the thermally induced stress in a shrinking pavement layer reaches the tensile strength of asphalt, regularly spaced thermal cracks form across the width of the pavement. A one-dimensional analytical solution for the stress distribution in a thermally shrinking elastic pavement layer placed on an elastoplastic, cohesive–frictional base is developed and validated by comparison with a 2D numerical solution. From the analytical model, a prediction of a length parameter that provides bounds on the thermal crack spacing is obtained. Predicted bounds on crack spacing are validated by comparison with field observations. It is demonstrated that the proposed formulation can also be applied to estimate the average crack density observed in thin ceramic films subjected to the application of an axial strain; in the latter system, the crack spacing is six decades smaller than that observed in pavement systems.

Keywords: Thin films; Pavements; Coatings; Crack spacing; Thermal cracking

1. Introduction

When natural and engineered systems are subjected to shrinkage—driven by cooling or drying—the resulting stresses may lead to the formation of cracks. In many cases these cracks form patterns, which exhibit distinct length scales. The drying of mud is a classic example of this phenomenon (Bejan, 1999; Gabrielli et al., 1999; Horgan and Young, 2000). A keen area of research in engineered systems looks at the cracking patterns in thin films. When thin glass strips are exposed to a thermal gradient (Ronsin and Perrin, 1997) or thin colloidal suspensions are dried (Boeck et al., 1999), uniformly spaced longitudinal cracks form parallel to the direction of the temperature or moisture gradient. Alternatively, when thin film coatings are subjected to the application of an axial strain (which can be caused by a thermal or drying shrinkage) transverse cracks, normal to the direction of the applied strain, form at regular intervals (Agrawal and Raj, 1989; Su et al., 1998; Chen et al., 1999, 2000; Handge et al., 2001).

The focus of this paper is the development of a mathematical model to predict the length scale for the spacing of transverse cracks that form in a coating subjected to an axial strain. In a departure from previous

* Corresponding author. Tel.: +1-612-626-0789; fax: +1-612-626-7750.
E-mail address: guzina@wave.ce.umn.edu (B.B. Guzina).

0020-7683/02/$ - see front matter © 2002 Elsevier Science Ltd. All rights reserved.
PII: S0020-7683(02)00496-1

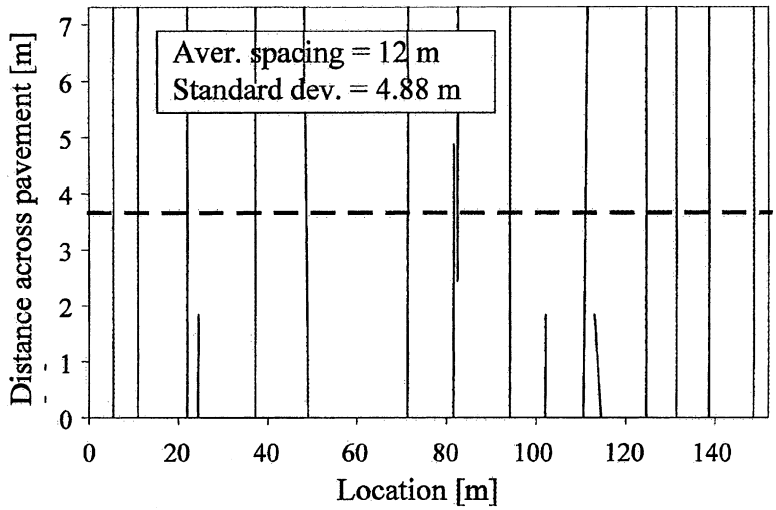

Fig. 1. Thermal cracking map of an asphalt pavement section.

work in this area (Agrawal and Raj, 1989; Chen et al., 1999, 2000), our engineering motivation for the study is not an improved understanding of thin film coatings but an understanding of how so-called thermal cracks, a feature of cold climates, form in asphalt pavements placed on a granular base (Marker, 1966; Zube, 1966; Kelley, 1966; Hills and Brien, 1966; Hiltunen and Roque, 1994; Timm, 2001). Typically, these cracks form after an extreme cooling event and extend across the width of the pavement. Such cracks not only affect the ride quality of the pavement, but also allow for the infiltration of water, which results in a rapid deterioration of the pavement structure. Fig. 1 illustrates a typical thermal cracking pattern observed on a section (150 m long and 7.5 m wide) of interstate road in Minnesota; these cracks formed in a single cooling event in the winter of 1996 when the surface pavement temperature dropped below −30 °C.

The central contribution of this paper is the development of an analytical one-dimensional model that predicts bounds on the thermal crack spacing in a cooled section of asphalt pavement. In this development it is assumed that a Winkler-type foundation (Hetenyi, 1946), augmented by a cohesive–frictional interface, can be used to model the interaction between the asphalt pavement and its granular base. The resulting model is validated by comparison with a 2D finite difference analysis and field observations of thermal cracks in asphalt pavements.

Although thermal cracking of pavements occurs at a larger scale than the cracking of thin films (meters as opposed to micrometers), the fundamental problem components are the same, i.e. a relatively thin coating (the asphalt lift) placed on a thicker substrate (the granular base) subjected to an axial strain. As such, it is expected that the pavement thermal cracking model should also be applicable to situations involving thin film coatings. This point is demonstrated, at the conclusion of the paper, by using the model to successfully predict the average crack spacing observed in titanium nitride (TiN) ceramic coatings subjected to an applied axial strain (Chen et al., 1999, 2000); a problem where the crack spaces are six orders of magnitude smaller than those found in pavements.

2. Formulation of the problem

To examine the fundamental nature of thermal cracking in pavement systems, it is useful to consider the distribution of thermal stresses in an elastic strip (length λ, width w, thickness h, Young's modulus E,

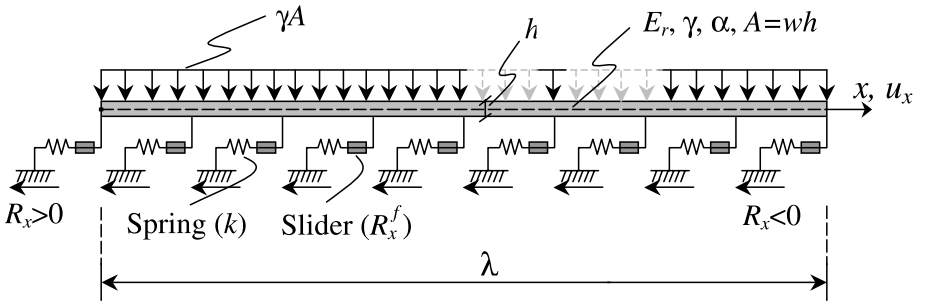

Fig. 2. Elastic rod resting on an elastoplastic foundation.

Poisson's ratio v, coefficient of thermal expansion α, and unit weight γ) subjected to a negative temperature change $\Delta T < 0$ while resting upon a dissimilar elastoplastic solid (herein referred to as the base). In this set up, it is assumed that the asphalt is sufficiently cooled so that viscous effects can be neglected. Further, to reflect the granular or clayey make up of the base layer, shear stresses in the base are assumed to be limited from above according to the Mohr–Coulomb failure criterion.

Under the assumption of negligible transverse tensile stress in the cooling layer, an analytical treatment of the foregoing problem can be obtained by approximating the system by an elastic rod with Young's modulus $E_r = E$, restrained axially by a Winkler-type foundation (e.g. Hetenyi, 1946). To allow for the slippage between the rod and the base, the Winkler foundation is augmented by a cohesive–frictional interface, as indicated schematically in Fig. 2, via slider elements interposed between the rod and the spring units. In what follows, it is assumed that the rod is sufficiently thin so that the bending effects due to the eccentric nature of the Winkler-type restraint can be neglected. On denoting the axial displacement in the rod by u_x, the reaction per unit length of the augmented Winkler foundation can be formally written as

$$R_x(x) = \begin{cases} ku_x, & |u_x| < R_x^f/k, \\ R_x^f \operatorname{sign} u_x, & |u_x| \geqslant R_x^f/k, \end{cases} \quad 0 \leqslant x \leqslant \lambda \tag{1}$$

for the case of monotonic thermal loading, where k stands for the elastic spring coefficient (dimension force/length^2), and R_x^f is the maximum shear resistance sustained by the sliders. In the spirit of the Mohr–Coulomb failure criterion, R_x^f is taken as

$$R_x^f = w\tau_f = w(c + p_z \tan\phi) = w(c + \gamma h \tan\phi), \quad 0 \leqslant x \leqslant \lambda, \tag{2}$$

where τ_f is the interfacial shear stress at failure, $p_z = \gamma h$ is the normal stress exerted on the Winkler foundation due to the weight of the rod, and c and ϕ denote the cohesion and friction angle of the base material, respectively.

With reference to Fig. 2, application of a uniform temperature change $\Delta T < 0$ to the rod results in its net shrinkage and the subsequent development of shear stresses along the rod–base interface. Depending on ΔT, the resulting reaction of the base can be either purely elastic or elastoplastic. Solutions for the stress distribution, for both cases, are developed below. On noting the symmetry of the problem, which requires that $u_x(\lambda - x) = -u_x(x)$, these analyses will be focused on the half-rod domain, $0 \leqslant x \leqslant \lambda/2$.

3. Restrained rod model I: elastic support

Under the assumption that the longitudinal displacements in the rod are sufficiently small so that the foundation resistance is purely elastic, the equilibrium equation governing the rod response due to cooling can be written as

$$\frac{\mathrm{d}\sigma_x}{\mathrm{d}x} = \frac{ku_x}{wh}, \quad 0 \leqslant x \leqslant \lambda/2, \tag{3}$$

where k is the spring coefficient of the base foundation. With the aid of the uniaxial thermoelastic constitutive relation for the rod, namely

$$\sigma_x = E_\mathrm{r}\left(\frac{\mathrm{d}u_x}{\mathrm{d}x} - \alpha\Delta T\right), \quad 0 \leqslant x \leqslant \lambda/2 \tag{4}$$

the general solution to (3), in terms of u_x, can be written as

$$u_x(x) = C_1\mathrm{e}^{\beta x} + C_2\mathrm{e}^{-\beta x}, \quad \beta = \sqrt{\frac{k}{E_\mathrm{r}A}}, \quad 0 \leqslant x \leqslant \lambda/2, \tag{5}$$

where $A = wh$ denotes the cross-sectional area of the rod, and C_1 and C_2 are the constants of integration. On imposing the boundary conditions $\sigma_x(0) = 0$ and $u_x(\lambda/2) = 0$, the distribution of thermally induced axial displacements and stresses in the elastically supported rod can be shown, by virtue of (4) and (5), to admit the representation

$$\begin{aligned} u_x(x) &= \frac{\alpha\Delta T}{\beta(1+\mathrm{e}^{-\beta\lambda})}(\mathrm{e}^{-\beta(\lambda-x)} - \mathrm{e}^{-\beta x}), \\ \sigma_x(x) &= E_\mathrm{r}\alpha\Delta T\left\{\frac{1}{1+\mathrm{e}^{-\beta\lambda}}(\mathrm{e}^{-\beta(\lambda-x)} + \mathrm{e}^{-\beta x}) - 1\right\}, \quad 0 \leqslant x \leqslant \lambda/2. \end{aligned} \tag{6}$$

On the basis of (6a), the restriction on the no-slip assumption, namely $ku_x(0) < R_x^f$, can be written explicitly as

$$\lambda < \begin{cases} \infty, & \eta \geqslant 1, \\ \dfrac{1}{\beta}\log\left(\dfrac{1+\eta}{1-\eta}\right), & \eta < 1, \end{cases} \quad \eta = \frac{\beta\tau_\mathrm{f}w}{k\alpha(-\Delta T)}. \tag{7}$$

Eq. (7) quantifies an intuitive notion of the threshold interface strength $\tau_\mathrm{f} = \eta k\alpha(-\Delta T)/(\beta w)$ that would, for a given thermal loading, preclude the occurrence of the rod-foundation slip regardless of λ.

In Fig. 3, the distribution of thermal stresses in the rod is plotted as a function of the segment length λ and the foundation-rod stiffness ratio β. From the display, it can be seen that the rate of change of axial stress in the rod (barring any interfacial slip) near the free ends increases with the normalized foundation

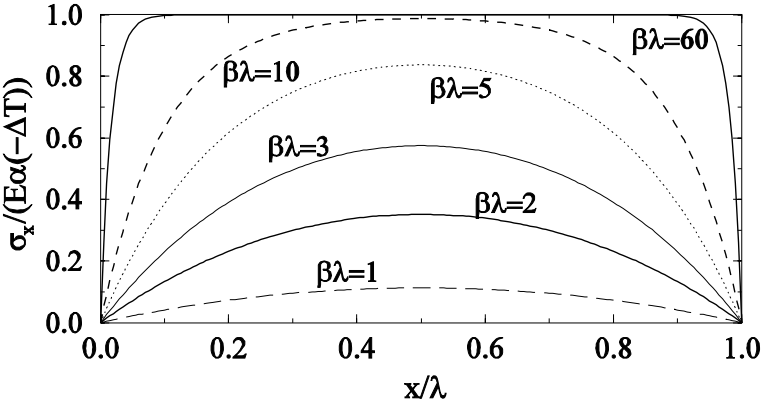

Fig. 3. Distribution of thermal stresses in a restrained rod: elastic case.

stiffness β. For further reference, one may also note from (6b) that the maximum tensile stress in the rod for the case of elastic resistance is given by

$$\sigma_{x,\max} = \sigma_x(\lambda/2) = E_r \alpha \Delta T \left\{ \frac{1}{\cosh(\beta\lambda/2)} - 1 \right\}. \tag{8}$$

4. Restrained rod model II: elastoplastic support

In situations when the rod length exceeds the limit for the elasticity assumption given by (7), thermally induced reaction of the Winkler foundation in Fig. 2 can be divided into two distinct areas, namely (i) the sliding region, and (ii) the non-slip, i.e. elastic reaction zone as shown in Fig. 4. In region I ($0 \leqslant x < x_t$), axial displacements in the rod (u_x) are sufficient to cause slippage along the slider–spring support so that $R_x = R_x^f$, whereas region II ($x_t < x \leqslant \lambda/2$) is characterized by the elastic foundation resistance with $R_x = ku_x$.

4.1. Region I—sliding resistance

With reference to Fig. 4, axial stress in the rod for $x < x_t$ caused by the constant base reaction (2) can be shown to admit the linear representation

$$\sigma_x(x) = \frac{\tau_f}{h} x = \left(\frac{c}{h} + \gamma \tan\phi \right) x, \quad 0 < x < x_t \tag{9}$$

from which it is apparent that the rate of increase of axial stress in region I is directly proportional to the maximum shear resistance (τ_f) of the Winkler-type foundation.

4.2. Region II—linear elastic resistance

Owing to the presence of axial restraint, it is reasonable to expect the existence of an interior region in the rod away from the free end ($x_t < x \leqslant \lambda/2$) where the longitudinal displacements in the thermally shrinking rod are sufficiently small so that $u_x < R_x^f/k$. Following the earlier developments, the solution for region II can be written as

$$u_x(x) = C_1 e^{\beta x} + C_2 e^{-\beta x}, \quad \beta = \sqrt{\frac{k}{E_r A}}, \quad x_t < x \leqslant \lambda/2. \tag{10}$$

To determine C_1 and C_2, one may observe with reference to Fig. 4 that

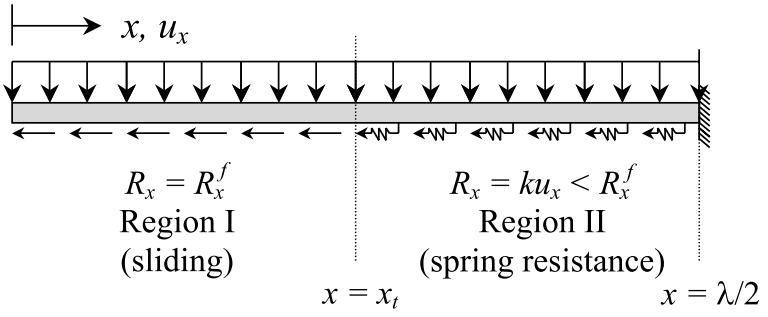

Fig. 4. Reaction of the Winkler-type foundation due to uniform cooling of the rod.

$$u_x(x_t^+) = \frac{\tau_f w}{k}, \quad u_x(\lambda/2) = 0, \tag{11}$$

where the first equation indicates that the composite Winkler foundation is on the verge of failure at the transition point. In applying the Dirichlet boundary conditions (11), however, it should be noted that the position of transition $x = x_t$ is unknown a priori. To establish an additional equation necessary for the solution of the problem, it is instructive to invoke the continuity of axial stresses in the rod, which, through (9), requires that

$$\sigma_x(x_t^+) = \sigma_x(x_t^-) = \frac{\tau_f x_t}{h}. \tag{12}$$

By virtue of (4) and (10)–(12), the axial displacement and stress fields in region II can be solved as

$$\begin{aligned} u_x(x) &= \frac{\alpha\Delta T(1-\beta\eta x_t)}{\beta(e^{-\beta(\lambda-x_t)} + e^{-\beta x_t})}(e^{-\beta(\lambda-x)} - e^{-\beta x}), \\ \sigma_x(x) &= E_r\alpha\Delta T\left\{\frac{1-\beta\eta x_t}{e^{-\beta(\lambda-x_t)} + e^{-\beta x_t}}(e^{-\beta(\lambda-x)} + e^{-\beta x}) - 1\right\}, \quad x_t < x \leqslant \lambda/2, \end{aligned} \tag{13}$$

where β is defined in (10), and x_t is given by the implicit formula

$$x_t = \frac{\lambda}{2} - \frac{1}{2\beta}\log\left(\frac{1-\beta\eta x_t + \eta}{1-\beta\eta x_t - \eta}\right), \quad 0 < \eta < 1, \quad 0 < x_t < \lambda/2. \tag{14}$$

Eq. (14) can be solved via the bisection method.

On the basis of (9) and (13), the axial stress distribution in the rod for the elastoplastic case takes the characteristic form of an initial linear portion and an exponential "cap" as pictured in Fig. 5. As can be seen from the display, an increase in the normalized foundation strength η effectively increases the axial stress in the rod and shortens region I. Conversely, an increase in the normalized elastic stiffness β of the Winkler foundation can be shown to inherently accelerate an exponential approach towards the maximum stress in the rod given by

$$\sigma_{x,\max} = \sigma(\lambda/2) = E_r\alpha\Delta T\left\{\frac{1-\beta\eta x_t}{\cosh(\beta(\lambda/2 - x_t))} - 1\right\}. \tag{15}$$

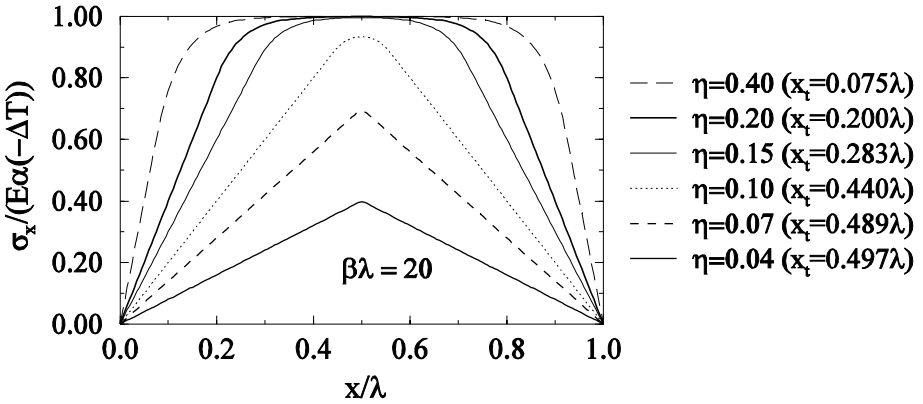

Fig. 5. Distribution of thermal stresses in a restrained rod: elastoplastic case.

5. Thermal gradient correction

Owing to its reduced dimensionality, the analytical model described above makes no provision for the presence of thermal gradients across the layer thickness. As a result, the temperature change ΔT in the 1D formulation inherently refers to the mid-fiber of the surface layer. Depending on the rate of cooling, however, a noticeable temperature difference, $T_1 < T_2 < T_0$ may develop across the pavement layer thickness as depicted in Fig. 6. In such situations, it is possible to consistently account for the thermal gradient by adding the bending stress contribution to the mid-fiber solutions (6b), (9) and (13b) as a means to estimate the maximum stress in the extreme top fiber. This bending stress correction, which accounts for a temperature difference, can be calculated as $E_r\alpha(T_2 - T_1)/2$, yielding the following expressions for the axial stress in the *top fiber* of the rod

$$\sigma_x^{\text{top}}(x) = \begin{cases} \left(\dfrac{c}{h} + \gamma_t \tan\phi\right)x + \dfrac{E_r\alpha(T_2 - T_1)}{2}, & 0 \leqslant x \leqslant x_t, \\ E_r\alpha\Delta T\left\{\dfrac{1 - \beta\eta x_t}{e^{-\beta(\lambda - x_t)} + e^{-\beta x_t}}(e^{-\beta(\lambda - x)} + e^{-\beta x}) - 1\right\} + \dfrac{E_r\alpha(T_2 - T_1)}{2}, & x_t \leqslant x \leqslant \lambda/2. \end{cases} \tag{16}$$

These equations are applicable to both no-slip (i.e. $x_t = 0$) and partial slip ($x_t > 0$) interfacial conditions. With reference to (8) and (15), the maximum stress in the rod that accounts for the existence of thermal gradients can be written jointly as

$$\sigma_{x,\max}^{\text{top}} = \sigma_{x,\max} + \frac{E_r\alpha(T_2 - T_1)}{2}. \tag{17}$$

Note that a model that is similar to (16), although without an account for the thermal gradients, has been recently presented by Zhang and Li (2001) for the shrinkage-induced stresses in concrete pavements.

The relationship in (16) was developed under the plain stress condition (i.e. zero lateral restraint in the top layer). By accounting for the Poisson's effect, however, it can also be applied to plane strain problems through the definition of an effective Young's modulus of the rod, E_r (e.g. Malvern, 1969). On associating $\alpha\Delta T$ in (16) with the concept of initial strain (see Zienkiewicz and Taylor, 1989), such a generalization can be effected by writing

$$E_r = \begin{cases} E, & \text{plane } \textit{stress} \text{ condition in the top layer subject to isotropic initial strain,} \\ \dfrac{E}{1 - \nu}, & \text{plane } \textit{strain} \text{ condition in the top layer subject to isotropic initial strain,} \\ \dfrac{E}{1 - \nu^2}, & \text{plane } \textit{strain} \text{ condition in the top layer subject to axial initial strain,} \end{cases} \tag{18}$$

where E and ν denote the Young's modulus and Poisson's ratio of the top layer, respectively.

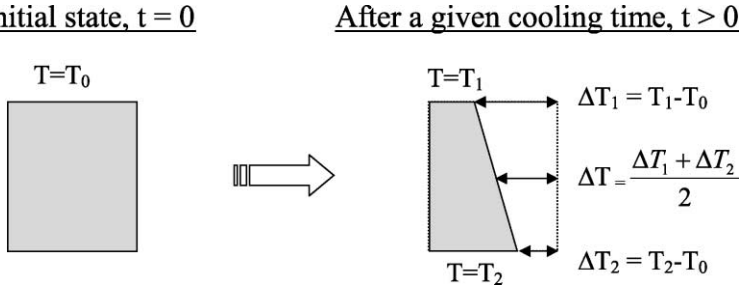

Fig. 6. Temperature variation across thickness of the pavement layer.

6. Calculation of the foundation stiffness

The applicability of the proposed approach, to a given situation, rests on establishing an appropriate expression for the Winkler foundation stiffness, manifest in the parameters k or β. A general treatment is to consider a benchmark system and restrict k in the restrained rod model to match its overall stiffness to that of the benchmark system. For the pavement cooling problem, an optimal benchmark would be that of an elastic half-space or stratum subjected to self-equilibrating shear surface tractions distributed over a rectangular area. Unfortunately, this problem does not have a closed-form solution and alternative benchmarks need to be sought.

One convenient choice for a benchmark suited for the pavement cooling problem is the plane-strain model illustrated in Fig. 11a of Appendix A. With reference to the Figure, matching the quarter-span horizontal displacements of the half-plane model to that of the Winkler foundation (see Appendix A) yields

$$\beta = \sqrt{\frac{k}{E_r A}} = \sqrt{\frac{4\pi E_b}{\lambda h E_r (1-\nu_b^2)(4+3\log 3)}\left(1+\frac{(4+3\log 3)(1-\nu_b)}{8\pi}\,\frac{\lambda}{h_b}\right)}, \tag{19}$$

where E_b and ν_b denote the Young's modulus and Poisson's ratio of the base, respectively. The last component in (19) is a "correction" term that accounts for situations where the base is an elastic stratum of finite thickness, h_b. It is introduced by interpolating between the available limiting solutions for $\lambda/h_b \to 0$ (i.e. half plane) and $h_b/\lambda \to 0$ (shallow stratum).

7. Comparison with 2D simulations

To evaluate the ability of the proposed analytical model to simulate the axial stress distribution in a thin layer supported by a cohesive-frictional *continuum*, a comparison is made with a plane-strain numerical simulation, generated via a commercially available finite difference code, FLAC (Coetzee et al., 1995). The 2D model geometry and boundary conditions are illustrated in Fig. 7, with the top layer fully bonded to the base. In contrast to the top layer, which is modeled as an elastic material, the constitutive behavior of the base layer is assumed to be elastoplastic with an associated flow rule according to the Mohr–Coulomb model. This model is characterized by the Young's modulus E_b, Poisson's ratio ν_b, cohesion c, and the angle of internal friction ϕ. To expose the effects of *relative* thermal shrinkage, the coefficient of thermal expansion for the base material, α_b, is set to zero in the (numerical) cooling experiment.

The data for the comparison between the 1D analytical and 2D numerical model is given in the first two columns of Table 1. The entries are consistent with values that might be found in an asphalt pavement placed on a dry granular base (Timm, 2001). Following earlier developments, the Young's modulus of the rod for the 1D model is calculated via (18b), where E and ν denote the Young's modulus and Poisson's ratio

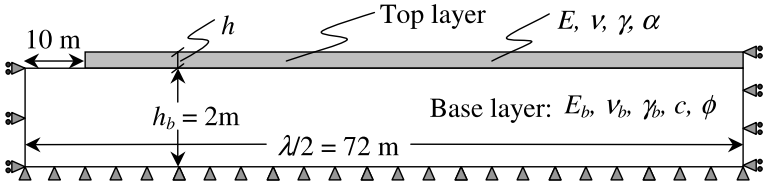

Fig. 7. 2D finite difference model.

Table 1
Pavement data

Value	Fig. 8	Fig. 9	Table 2
E	14.0 GPa	6.9 GPa	14.0 GPa
v	0.20	0.35	0.20
γ	21.6 kN/m^3	21.6 kN/m^3	21.6 kN/m^3
α	2.15×10^{-5} 1/K	1.0×10^{-5} 1/K	1.8×10^{-5} 1/K
S	–	–	1.9 MPa
h	0.15 m	0.30 m	0.15 m
w	1.0 m	1.0 m	7.5 m
E_b	0.55 GPa	0.275 GPa	5.5 GPa
v_b	0.4	0.4	0.4
γ_b	19.6 kN/m^3	19.6 kN/m^3	–
c	10 kPa	0	15 kPa
ϕ	20°	70°	30°
h_b	2.0 m	2.0 m	2.0 m
ΔT	−5.0 K	−2.5 K	−15.0 K
$T_2 - T_1$	0 K	4.17 K	8.0 K

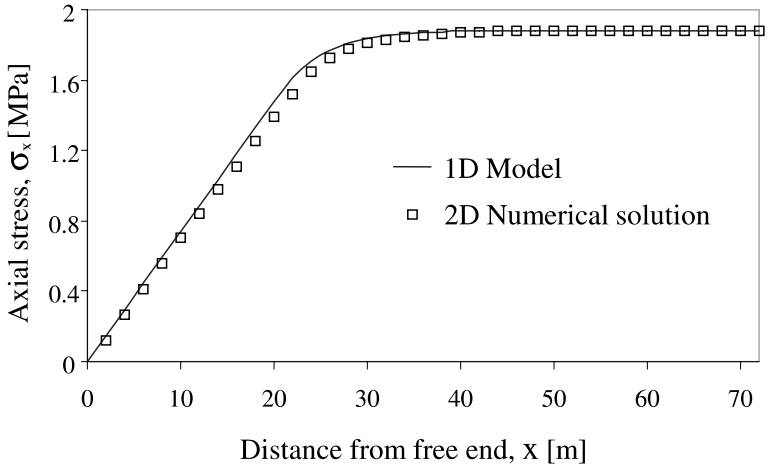

Fig. 8. Comparison between 1D and 2D solutions with no temperature gradient.

of the top layer in the plane-strain solution, respectively. A typical comparison for the case with no temperature difference (i.e. $T_1 = T_2$) in the top layer is illustrated in Fig. 8. The result clearly shows the ability of the analytical model to approximate thermal stress distribution in a pavement continuum. One may also observe that the conditions assumed in the figure are such that the transition from the plastic to elastic foundation response occurs at $x = x_t \sim 20$ m. A sample comparison between the 1D analytical model (16) and the 2D numerical solution for the case involving a temperature difference across the layer thickness is shown in Fig. 9. The response of the base in this case remains fully elastic. Once again, despite the simplifications underlying the analytical model, agreement with the numerical results is reasonable. Further, Fig. 9 illustrates the importance of accounting for the thermal gradient on comparing the top and mid-fiber solutions.

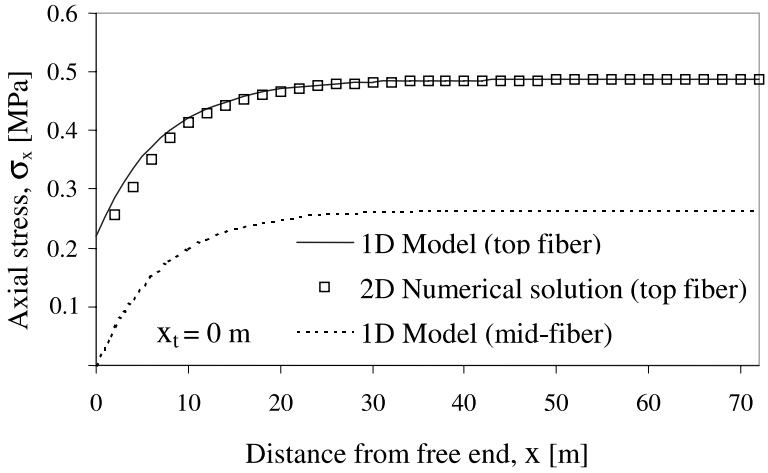

Fig. 9. Comparison between 1D and 2D solutions with temperature gradient.

8. Prediction of bounds on crack spacing

The results derived in previous sections provide, for a given temperature drop ΔT, the value of the maximum stress in a pavement section of length λ. This analysis, however, can also be used in an inverse sense to provide for a given ΔT, the section length, λ_s, for which the maximum thermal stress reaches the tensile strength of the pavement, S. Below it is shown that this length scale can be used to provide bounds on the crack spacing in an initially undamaged pavement section of arbitrary length L, subjected to thermal shrinkage.

Consider an initially undamaged pavement section of length L. The pavement is cooled through a temperature drop ΔT at its mid-fiber, with a possible thermal gradient across its thickness. If at any time during the cooling process, the axial stress in the top pavement fiber (σ_x^{top}) reaches the given tensile strength S, a crack will form. In the absence of material flaws, symmetry considerations suggest that the crack will form at the mid point, splitting the undamaged section into two equal parts. For simplicity of presentation, it will be assumed that the stress distribution in the newly created undamaged sections can be approximated via (16) with λ corresponding to the (new) intact segment length. With subsequent cooling, the cracking and subdividing of the pavement section will continue until the maximum tensile stress between two neighboring cracks falls below the strength S. At this point the crack spacing, equidistant along L, will take the value $L/(n+1)$ where $n \geqslant 0$ is the total number of cracks that have formed. If at any stage in the cracking process the crack spacing is larger than λ_s, then, by definition of λ_s, the maximum stress $\sigma_{x,\max}^{\text{top}}$ in each subsection would reach the tensile strength S and additional cracking and sub-division will occur. Clearly the new spacing that results from this additional sub-division will be larger than $\lambda_s/2$. On the other hand, if the spacing is less than λ_s, the maximum stress will be below the tensile strength and further cracking cannot be achieved. Hence for an arbitrary section with initial length $L > \lambda_s$, the final crack spacing achieved, λ_o, will be bounded by

$$\frac{\lambda_s}{2} < \left(\lambda_o = \frac{L}{n+1}\right) < \lambda_s \Rightarrow \bar{\lambda}_o = 0.75\lambda_s, \tag{20}$$

where $\bar{\lambda}_o$ denotes the *average* crack spacing. Note that (20), similar to an expression proposed by Agrawal and Raj (1989) for ceramic coatings, does not account for residual stresses and is therefore strictly valid

only in the limit cases of a pure elastic or rigid plastic base support. It is expected, however, that (20) can also be used, as a first-order approximation, for intermediate cases involving elastoplastic support. Below, this hypothesis will be tested against the published experimental data.

8.1. Solution for the length scale λ_s

On taking the limit of (8), (15) and (17) as $\lambda \to \infty$, one may observe that, for a given ΔT, cracking of a pavement section is possible only if

$$\psi \equiv \frac{S - \frac{\alpha E(T_2 - T_1)}{2}}{\alpha(-\Delta T)E} < 1. \tag{21}$$

With such an assumption and the requirement $\sigma^{\text{top}}_{x,\max} = S$, the length scale λ_s for the non-slip case can be derived from (8) and (17) as

$$\lambda_s = \frac{2}{\beta} \log\left(\frac{1 + \sqrt{2\psi - \psi^2}}{1 - \psi}\right) \tag{22}$$

provided that

$$\lambda_s < \begin{cases} \infty, & \eta \geqslant 1, \\ \dfrac{1}{\beta} \log\left(\dfrac{1+\eta}{1-\eta}\right), & \eta < 1 \end{cases} \tag{23}$$

with η given by (7). For any given combination of material parameters governing the rod response, inconsistency of (22) and (23) implies the necessity of employing the elastoplastic solution in calculating λ_s. On the basis of (15) and (17), the partial slip solution can be shown to yield

$$\lambda_s = 2x_t + \frac{2}{\beta} \log\left(\frac{1 + \sqrt{1 - \left(\frac{1-\psi}{1-\beta\eta x_t}\right)^2}}{\frac{1-\psi}{1-\beta\eta x_t}}\right). \tag{24}$$

It should be noted that x_t in (24) depends in turn on $\lambda = \lambda_s$ via (14). Moreover, the value of the relative foundation stiffness β, given by (19), is intrinsically dependent on the choice of the representative rod length, which is for consistency taken as $\lambda = 2\lambda_s$, i.e. the maximum intact segment length just before the terminal subdivision (i.e. cracking) event that results in λ_s as given by (22) or (24). Hence a recursive solution is required to determine the length scale in situations involving both no-slip and partial slip between the rod and its foundation.

8.2. Limits on the length scale

In the limit as $\Delta T \to -\infty$, the values η and ψ (see (7) and (21)) both approach zero, and the crack spacing (24) reaches the limiting value $\lambda_s \to 2x_t$ from above. In this limit, the slip zone will extend the entire inter-crack space, and from (16a) it can be determined that, for a given thermal difference $T_2 - T_1$ across the pavement thickness,

$$\lambda_s^{\lim} = \frac{\{2S - \alpha E(T_2 - T_1)\}h}{\tau_f} \tag{25}$$

is a lower bound, independent of ΔT, on the crack spacing length scale. Depending on the geometric and material properties in a pavement system, this full-slip limit can be approached at relatively moderate mid-fiber values of axial strain, $\varepsilon = E\alpha(-\Delta T)$. On employing the definition $\beta = \sqrt{k/(E_r A)}$ and (24), it is also interesting to observe that, for any $\Delta T < 0$, (25) *simultaneously* represents the limit of λ_s as the base stiffness approaches infinity, i.e. $k \to \infty$.

8.3. Comparison with pavement field data

A critical test for the proposed model of thermal cracking is to compare (19) through (24) with field observations. Particular emphasis is placed on obtaining theoretical bounds which match the order of the crack spacing observed in the field. Timm (2001) carried out a statistical analysis of pavement sections at the Minnesota Road (Mn/ROAD) testing facility. A cracking map from one of these test sites is shown in Fig. 1. The average spacing and standard deviations for the three sections (which all have asphalt thickness $h = 0.15$ m) are given in Table 2; the observed scatter can be explained in terms of a distribution of flaws in the actual pavement structure.

Appropriate material data for the analysis of field test sections are given in the last column of Table 1. It should be noted that in this field study the granular base was wet and frozen, which accounts for the high value of the base Young's modulus, E_b. The value of $\Delta T = -15$ K corresponds to the measured maximum daily temperature change during the time that the cracks appeared in the pavement, and the value of $T_2 - T_1 = 8$ K is temperature drop across the pavement thickness, provided by thermocouple measurements. A full rational and sources used in the choice of the data in Table 1 are documented in Timm (2001). Substitution of the values in Table 1 into (19)–(24) yields the crack spacing length scale $\lambda_s = 15.92$ m; as a result, the predicted bounds on the crack spacing are

$$7.96 \text{ m} < \lambda_o < 15.92 \text{ m}. \tag{26}$$

Thus the proposed model provides coverage of the field observed values (see Table 2) and the crack spacing predictions match the order of those observed in the field.

In (26), the benchmark model used to determine the Winkler foundation stiffness is the plane strain model (19), which would underestimate k derived from a more refined 3D benchmark solution for an elastic stratum involving surface tractions distributed over a rectangular area. It should be noted, however, that due to the frozen and stiff nature of the base, the crack-spacing result in (26) is close to its rigid-base (saturation) limit stemming from (25), namely

$$7.93 \text{ m} < \lambda_o^{\text{sat}} < 15.86 \text{ m}. \tag{27}$$

As a result, the use of three-dimensional elastostatic benchmarks as a tool to estimate k, which would geometrically be more appropriate for the problem of interest, would only reduce already minor differences between (26) and (27).

Table 2
Field observed crack spacing

Cell	Average spacing (m)	Standard deviation (m)
1	12	4.88
2	8	4.27
3	13	8.23

9. Thin films

Although the prior analysis has been constructed for the case of a thermally shrinking asphalt pavement placed on a cohesive-frictional base, the featured thermal crack spacing model (19)–(24) should also be applicable to the case of thin elastic films on a strained ductile metal substrate. This contention is supported by research in the thin film area where a slip zone near the cracks has been hypothesized (Hu and Evans, 1989).

In order to extend the thermal crack model to the thin film case, the friction angle of the base is set to zero, i.e. $\phi = 0$ so that the cohesion c can be identified with the ultimate shear strength of the metal substrate (Chen et al., 1999, 2000).

To demonstrate the thin film application of the thermal cracking model, it is useful to consider the experimental set up reported by Chen et al. (1999, 2000) of a titanium-nitride (TiN) ceramic coating deposited on a 304 stainless steel "dog bone" substrate and subjected to an increasing axial strain. The geometric data for the experimental set up is given in Table 3 where H, λ, and w refer to the thickness, length, and width of the notched section of the substrate, respectively.

In addition to the geometric experimental conditions, material properties of the composite specimen also need to be specified before the thermal crack model (19)–(24) can be implemented. The three critical material properties, also listed in Table 3, are:

1. *Ultimate shear strength*, τ_f: Under the assumption that the strength of the interface between the film and substrate is higher than that the metal substrate, the ultimate shear strength is set at $\tau_f = 0.233$ GPa. This value, as noted by Chen et al. (2000), is consistent with the yield strength of steel.
2. *Residual stress*, σ_{res}: As a result of the TiN deposition process, a significant compressive residual stress, σ_{res} may be present in the coating (e.g. Shieu et al., 1998). As a result, the axial strain ε imposed on the TiN coating must be corrected to account for the residual stress. To this end, Su et al. (1998) and Chen et al. (2000) among others used the concept of an *effective* strain

$$\varepsilon_{eff} = \varepsilon - \frac{\sigma_{res}}{E}, \tag{28}$$

   where E is the Young's modulus of the coating. From measurements, Chen et al. (1999) report a value of $\sigma_{res} = 10.4$ GPa.
3. *Tensile strength of the film*, S: Chen et al. (2000) and other researchers (Su et al., 1998; Shieu et al., 1998) calculate the tensile strength of the film as $S = \varepsilon_{eff}^{thr} E$ using the threshold effective strain in the coating, ε_{eff}^{thr}, measured at the instant when cracks first appear. This approach, however, can be subjected to large errors (see further discussion below), and in the current effort an alternative self-consistent approach is used. In experimental works dealing with the cracking of thin films (Chen et al., 1999; Shieu et al., 1998),

Table 3
Experimental geometry and specimen properties after Chen et al. (1999, 2000)

h	1.3 μm
H	800 μm
λ	10 mm
w	10 mm
E	500 GPa
v	0.2
S	0.853 GPa
σ_{res}	10.4 GPa
E_b	190 GPa
v_b	0.3
τ_f	0.233 GPa

it is observed that as the strain is increased, the crack spacing decreases up to a saturation point. Beyond this saturation point, additional straining of the specimen does not result in a further decrease of crack spacing. This behavior is consistent with the identification of the full-slip limit length scale, $\lambda_s^{\lim}$, discussed above. Hence, if the average saturation spacing $\bar{\lambda}_o^{\text{sat}} = 0.75\lambda_s^{\lim}$ can be measured, the tensile strength of the film will follow immediately from (25), i.e.

$$S = \frac{2\bar{\lambda}_o^{\text{sat}}\tau_f}{3h} \tag{29}$$

under the assumption that ε_{eff} does not vary across the film thickness. In their experimental work, Chen et al. (1999) measure the average saturation crack spacing, below the point where spallation of the film occurs, of $\bar{\lambda}_o^{\text{sat}} = 7.143$ μm. This value used in (29) gives a tensile strength of $S = 0.853$ GPa.

9.1. Comparison with thin film data

Owing to the fact that the crack spacing in thin films is typically several orders of magnitude smaller than the specimen width, a common point of departure in the analysis of this class of problems is the assumption of plane strain for the mid-line of the specimen (e.g. Chen et al., 2000), where the cracks are monitored. To provide a basis for comparison, the crack spacing model developed in this study is applied to the thin film data with the rod's modulus E_r, foundation stiffness k and temperature "drop" ΔT given by (18c), (19), and $\alpha\Delta T = -(\varepsilon - \sigma_{\text{res}}/E_r)$, respectively. Consistent with the fact that the crack spacing in thin films is negligible compared to the substrate thickness, the ratio λ/h_b in (19) is set to zero.

Fig. 10 plots the variation of crack density (i.e. number of cracks per mm) in the TiN coating versus applied strain as calculated on the basis of (19)–(24) and Table 3. As a point of comparison, the experimental observations (see Fig. 1 in Chen et al., 1999) are also shown in the display. Despite slight over prediction, it is clear, without any attempt at fitting, that the thermal crack model (19)–(24) not only matches the order of the observed cracking density, but also follows the correct trend with increasing strain.

9.2. Estimation of the film's tensile strength

As noted earlier, an alternative to (29) for finding the tensile strain of the TiN coating, used in literature (Su et al., 1998; Shieu et al., 1998; Chen et al., 2000), is to apply the uniaxial Hooke's law at the instance when cracks first appear, i.e. to set

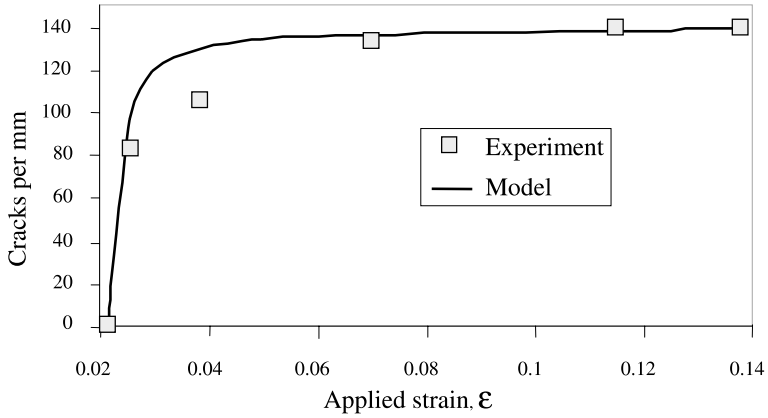

Fig. 10. Observed versus predicted crack density in 1.3 μm-thin TiN coating.

Table 4
Comparison of TiN tensile strength predictions

Paper	h (μm)	ε^{thr} (%)	λ_o^{sat} (μm)	σ_{res} (GPa)	τ_{f} (GPa)	E (GPa)	S (29) (GPa)	S (30) (GPa)
Chen et al. (1999, 2000)	1.3	2.54	7.143	10.4	0.233	500	0.853	2.4
Shieu et al. (1998)	1.0	4.00	8.333	12.8	0.233	640	1.294	12.8

$$S = E\varepsilon_{\text{eff}}^{\text{thr}} \equiv E\varepsilon^{\text{thr}} - \sigma_{\text{res}}. \tag{30}$$

With reference to Fig. 10, the main drawback in using this approach is that the crack density changes very rapidly near the onset of cracking, thus making it difficult to precisely identify the threshold strain, ε^{thr}, at which cracks first appear. Furthermore, in many systems the value of $E\varepsilon^{\text{thr}}$ and σ_{res} are of the same order. As such, small changes of ε^{thr} in (30) will produce large changes in the predicted values of S. This is illustrated in Table 4 by comparing the S values predicted by the saturation method (29) with values, taken from the literature, using the Hooke's law approach (30). As can be seen from the table, the predictions for S stemming from the Hooke's law approach (30) vary by a factor of 5 for essentially the same systems. In contrast, calculation of S from the saturation model (29) provides values of the same order. The later values could be considered to be low when compared with the Hooke's law estimates. Note, however, that Su et al. (1998), who have investigated the tensile strength of TiN coated cylinders in a similar manner to Chen et al. (1999, 2000) and Shieu et al. (1998), arrive at a value of $S = 0.24$ GPa. Hence the estimates of tensile strength based on (29) are within the range of values reported for TiN coatings.

10. Summary and conclusions

In this paper, a one-dimensional model consisting of an elastic rod restrained axially by an elastoplastic Winkler-type foundation was developed to predict the state of stress in a cooling pavement layer supported by a cohesive-frictional base. It was found that when a layer of finite length is cooled, a non-uniform stress field, increasing from the free ends and reaching a maximum at the center, results. The validity of the Winkler-type assumption for the rod–base interaction was confirmed by comparison of stress predictions with results from a two-dimensional numerical solution of an elastic layer supported by an elastoplastic continuum.

Use of the one-dimensional model led to the identification of the crack spacing length scale, λ_{s}, associated with a specified tensile strength, S, and temperature drop ΔT. The assumption that an initially undamaged section, subjected to cooling, continues to crack and subdivide until the maximum stress level between two adjacent cracks falls below the tensile strength S, resulted in bounds, in terms of λ_{s}, on the expected spacing of thermal cracks. Comparisons, using reported material data for pavement systems, with field observations of thermal cracks in pavements confirmed that the characteristic length obtained from the stress model is of the correct scale.

The utility and robust nature of the thermal crack model was underscored by demonstrating that the model is also suitable for predicting the average crack spacing in thin film coatings subjected to an increasing axial strain; a system that exhibits crack spaces that are six orders of magnitude smaller than those observed in pavements.

Appendix A. Calculation of the Winkler spring coefficient

In the absence of closed-form formulas describing the response of an elastic half-space due to lateral surface tractions distributed over a rectangular strip, a convenient benchmark that can be used for calibrating k is the corresponding plane-strain solution for a horizontal loading of "length" λ acting on a

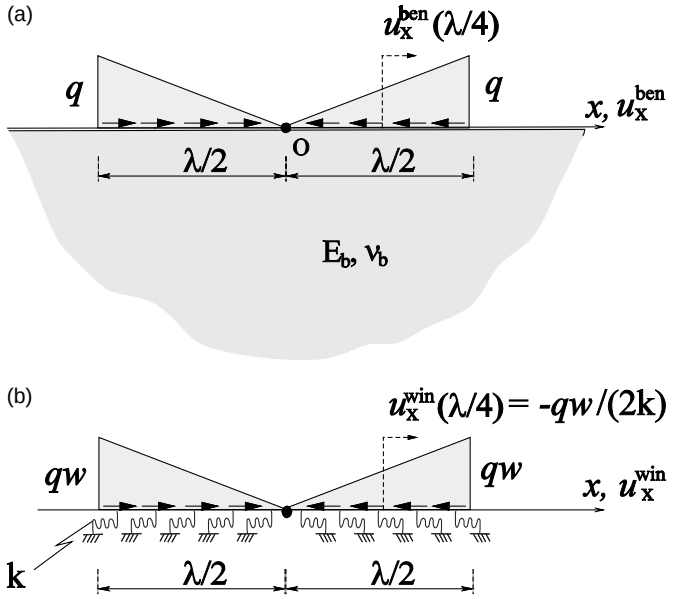

Fig. 11. Benchmark model for evaluating the spring coefficient k.

half-plane (see Fig. 11a). In the Figure, the shear tractions are assumed to follow a bi-linear distribution to mimic the self-equilibrating contact stresses between the shrinking pavement strip and its foundation. On employing the classical result in Poulos and Davis (1974) for the triangular variation of surface tractions, the solution for the horizontal surface displacement (u_x^{ben}) of the half-plane in Fig. 11a can be written as

$$u_x^{ben}(x) = \frac{q(1-\nu_b^2)}{\pi E_b}\left[\frac{4x^2-\lambda^2}{2\lambda}\log\left|\frac{\lambda+2x}{\lambda-2x}\right| - 2x\right], \tag{A.1}$$

where E_b and ν_b denote the Young's modulus and Poisson's ratio of the base material, respectively.

For comparison, Fig. 11b pictures the elastic Winkler foundation subjected to line loading which, calculated per width w of the plane-strain problem, corresponds to the contact stress distribution in Fig. 11a. To establish a similitude between the benchmark half-plane continuum and its Winkler-type analog, one may select k so that their respective quarter-span displacements are equal, i.e.

$$u_x^{ben}(\lambda/4) = u_x^{win}(\lambda/4). \tag{A.2}$$

On the basis of (A.1), (A.2) and the identity $u_x^{win}(\lambda/4) = -qw/(2k)$, the spring coefficient k approximating the continuum restraint for the shrinking pavement strip of length λ can be written as

$$k = \frac{4\pi E_b w}{\lambda(1-\nu_b^2)(4+3\log 3)}. \tag{A.3}$$

Beyond its direct relevance to the semi-infinite base continuum, formula (A.3) can also be used to synthesize the stiffness of an elastic *stratum* with finite depth h_b, provided that $\lambda \ll h_b$. In situations when $\lambda \gg h_b$, on the other hand, (A.3) inherently overestimates the well-known limiting value for shallow strata, namely $k = G_b w/h$ where G_b denotes the shear modulus of the elastic stratum supported rigidly from below. To provide a unifying representation of k that is appropriate for both limiting cases, (A.3) is modified by introducing a linear "correction" term, i.e.

$$k = \frac{4\pi E_b w}{\lambda(1-\nu_b^2)(4+3\log 3)}\left(1+\frac{(4+3\log 3)(1-\nu_b)}{8\pi}\frac{\lambda}{h_b}\right). \tag{A.4}$$

One may observe that the proposed correction for the stratum thickness, h_b, is similar in nature to the formulas describing the horizontal stiffness of a rigid foundation on an elastic stratum (Gazetas, 1991). Finally, it should be noted that even though k inherently depends on the rod width w via (A.4), the associated foundation-rod stiffness ratio β does not, since

$$\beta = \sqrt{\frac{k}{E_r A}} = \sqrt{\frac{4\pi E_b}{\lambda h E_r(1-\nu_b^2)(4+3\log 3)}\left(1+\frac{(4+3\log 3)(1-\nu_b)}{8\pi}\frac{\lambda}{h_b}\right)}. \tag{A.5}$$

References

Agrawal, D.C., Raj, R., 1989. Measurement of the ultimate shear strength of a metal–ceramic interface. Acta Metallurgy of Materials 37, 1265–1270.

Bejan, A., 1999. How nature takes shape: Extensions of constructal theory to ducts, rivers, turbulence, cracks, dendritic crystals and spatial economics. International Journal of Thermal Sciences 38, 655–663.

Boeck, T., Bahe, H.-A., Lampenscherf, S., Bahr, U., 1999. Self-driven propagation of crack arrays: A stationary two-dimensional model. Physical Review E 59, 1408–1416.

Chen, B.F., Hwang, J.F., Chen, Yu, G.P., Huang, J.H., 2000. A tensile-film-cracking model for evaluating interfacial shear strength of elastic film on ductile substrate. Surface and Coatings Technology 126, 91–95.

Chen, B.F., Hwang, J.F., Chen, Yu, G.P., Huang, J.H., 1999. In situ observation of the cracking behavior of TiN coating on 304 stainless steel subjected to tensile strain. Thin Solid Films 352, 173–178.

Coetzee, M.J., Hart, R.D., Varona, P.M., Cundall, P.A., 1995. FLAC Basics, Revised Edition. Itasca Consulting Group, Inc., Minneapolis, Minnesota.

Gabrielli, R., Cafiero, Caldarelli, G., 1999. Statistical properties of fractures in damaged materials. Europhysics Letters 45, 13–19.

Gazetas, G., 1991. Foundation Vibrations (Chapter 15). In: Fang, H.-Y. (Ed.), Foundation Engineering Handbook. Van Nostrand Reinhold, New York.

Handge, U.A., Sokolov, J.M., Blumen, A., 2001. Disorder and plasticity in fragmentation of coatings. Physical Review E 64, 1063–1067.

Hetenyi, M., 1946. Beams on Elastic Foundations. University of Michigan Press, Ann Arbor, MI.

Hills, J.F., Brien, D., 1966. The fracture of bitumens and asphalt mixes by temperature induced stresses. Proceedings, Association of Asphalt Paving Technologists 35, pp. 292–309.

Hiltunen, D.R., Roque, R., 1994. A Mechanics-based prediction model for thermal cracking of asphaltic concrete pavements. Association of Asphalt Paving Technologists 63, 81–117.

Horgan, G.W., Young, I.M., 2000. An empirical stochastic model for the geometry of two-dimensional crack growth in soil. Geoderma 96, 263–276.

Hu, M.S., Evans, A.G., 1989. The cracking and decohesion of thin films on ductile substrate. Acta Metallurgy of Materials 37, 917–925.

Kelley, J.E., 1966. Cracking of asphalt concrete pavements associated with volume changes in underlying materials and base courses. Proceedings, Association of Asphalt Paving Technologists 35, pp. 290–292.

Marker, V., 1966. Introduction to non-traffic load associated cracking of asphalt pavements. Proceedings, Association of Asphalt Paving Technologists 35, pp. 239–247.

Malvern, L.E., 1969. Introduction to the Mechanics of a Continuous Medium. Prentice Hall.

Poulos, H.G., Davis, E.H., 1974. Elastic Solutions for Soil and Rock Mechanics. John Wiley & Sons, New York.

Ronsin, O., Perrin, B., 1997. Multi-fracture propagation in a directional crack-growth experiment. Europhysics Letters 38, 435–440.

Shieu, F.S., Cheng, L.H., Sung, Y.C., Huang, J.H., Yu, G.P., 1998. Microstructure and coating properties of ion-plated TiN on type 304 stainless steel. Thin Solid Films 334, 125–132.

Su, Y.L., Yoa, S.H., Wei, C.S., Wu, C.T., 1998. Evaluation of the tension and fatigue behavior of various PVD coated materials. Thin Solid Films 322, 218–224.

Timm, D.H., 2001. A phenomenological model to predict thermal crack spacing of asphalt pavements. Ph.D. Thesis, University of Minnesota.

Zhang, J., Li, V.C., 2001. Influence of supporting base characteristics on shrinkage-induced stresses in concrete pavements. Journal of Transportation Engineering, ASCE 127, 455–462.

Zienkiewicz, O.C., Taylor, R.L., 1989. In: The Finite Element Method, vol. 1. McGraw-Hill, New York.

Zube, E., 1966. Cracking of asphalt pavements associated with absorptive aggregates. Proceedings, Association of Asphalt Paving Technologists 35, pp. 270–290.